THE JOURNAL OF PHYSICAL CHEMISTRY C

pubs.acs.org/JPCC Article

Nature of Reaction Intermediates and Origin of Bifunctionality in Manganese Oxide

Indroneil Roy, Qi Wang, and Vidhya Chakrapani*

Cite This: J. Phys. Chem. C 2020, 124, 5286–5299 Read Online

ACCESS | Metrics & More | Article Recommendations | Supporting Information

ABSTRACT: Bifunctional catalysts capable of catalyzing both oxygen reduction reaction (ORR) and oxygen evolution (OER) reaction are extremely valuable for oxygen-based energy conversion devices such as regenerative fuel cells and metal–air batteries. However, the underlying property of such catalysts that gives rise to their bifunctionality is not yet known nor explored. With the first use of near-infrared photoluminescence spectroscopy for tracking the changes in the individual metal cation valence states during electrocatalysis in combination with in situ gravimetric and resistance measurements, we show the underlying correlation between catalytic activity, potential-dependent resistance, and nature of reaction intermediates on various bifunctional and nonbifunctional surfaces. Our results show that bifunctional MnO_x reversibly switches electrical polarity from p-type to n-type along with the formation of high-valent cationic Mn^{4+} active sites as well as low-valent cationic Mn^{2+} active sites during OER and ORR, respectively, which is absent in nonbifunctional NiO and Co_3O_4. Results also show that other key process steps such as lattice hydration/dehydration occur during polarization. These results are rationalized in terms of a band structure framework which correlates electrochemical activity with the formation energy of various metal cation intermediates.

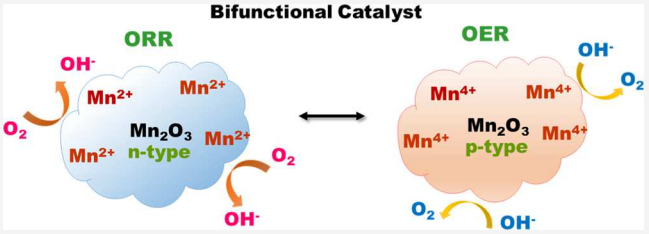

INTRODUCTION

Multifunctional catalysts capable of catalyzing multiple reactions on the same catalyst surface are of utmost importance for many chemical and energy transformations. For instance, in organic synthetic chemistry, bifunctional catalysts consist of complementary surface groups that work synergistically to enable both nucleophilic and electrophilic reactions and thereby lead to high-value molecular transformations compared to single-functional catalysts. In electrochemistry, bifunctional electrocatalysts are essential components of many reversible energy conversion and storage devices that enable the production of clean energy such as rechargeable metal–air batteries, and regenerative fuel cells, whose theoretical energy densities are on par with gasoline (~13 kW h/kg).[1] Considerable efforts have been dedicated toward improving the energy conversion efficiency of these devices,[2,3] but the main obstacle has been the lack of suitable bifunctional oxygen electrocatalysts that simultaneously show high activity for both oxygen reduction reaction (ORR) and oxygen evolution reaction (OER) during charge/discharge cycles.[4] The oxygen electrode is known to be strongly irreversible and consequently gives rise to large differences between the charging and discharging voltages, which leads to energy losses and decreased lifetimes of these systems. Some of the best-known electrocatalysts such as Pt, RuO_2, or IrO_2 are known to exhibit superior electrochemical activity for at least one of the electrolysis reactions [OER or ORR/HER (hydrogen evolution reaction)] but not both,[5−7] thus preventing their deployment as bifunctional electrocatalysts. While bifunctional activity has been reported on composite materials where OER and ORR occur on two compositionally different catalytic sites such as in Pt/Au[8] and Pt alloys,[9,10] N and P co-doped carbon,[11] Co_3O_4/carbon support,[12−14] very few pure catalysts are capable of simultaneous catalysis (single-site functionality) that is required for enhancing activity per unit area and minimizing transport and recombination losses. Semiconducting oxides of manganese (Mn_2O_3, MnOOH, and α-MnO_2)[15−17] and metallic oxides such as $LaNiO_x$,[18,19] doped (La or Cu) CoO_3[20−22] are single-site catalysts that have been reported to show OER/ORR bifunctionality.[17,23−26] This study focuses on understanding the underlying properties of semiconducting bifunctional oxides that are responsible for their single-site bifunctionality.

Prior in-depth evaluation of several phases of MnO_x by Dismukes and coworkers[27,28] and Ramirez and coworkers[25] have shown that α-Mn_2O_3 is the most active catalyst for OER, which was attributed to the presence of Mn^{3+} active sites in the corner-sharing MnO_6 octahedra as opposed to edge-sharing octahedrons.[27] Density functional theory calculations on α-Mn_2O_3 of Su et al. predicted HO*-covered Mn_2O_3 and O*-

Received: January 26, 2020
Revised: February 6, 2020
Published: February 21, 2020

https://dx.doi.org/10.1021/acs.jpcc.0c00714
J. Phys. Chem. C 2020, 124, 5286–5299

covered MnO_2 as the active sites for the ORR and the OER, respectively.[29] Experimental evidence for the predicted active sites has remained elusive. Systematic in-operando X-ray absorption spectroscopy (XAS) measurements have shown that the average oxidation state of Mn increases up to 3.4 during OER and decreases to 2.5 during ORR, as seen from the shifts of the absorption edge to either higher or lower energy.[30,31] One of the main limitations of X-ray-based techniques is that they can only provide information about the average oxidation state in strongly correlated oxides such as MnO_x, IrO_x, or NiO_x. This is because the strong spin−orbit and electrostatic interactions between the holes generated from the photoionization process from X-ray absorption and the unpaired valence-shell (d) electrons of high spin cations in strongly-correlated systems cause a severe broadening of photoelectron energies.[32] In a multivalent catalyst, the overlapping of broadened peaks of various oxidation-state cations makes the assignment of the oxidation state to a single identifiable peak energy in both XAS and X-ray photoelectron spectroscopy (XPS) very difficult. This loss of sensitivity makes individual chemical states in mixed valent oxide difficult to resolve.[33] This has led to ambiguities in the exact nature of Mn valent state that is responsible for the OER/ORR activities. While the determination of the relative contribution of different metal oxidation states (such as Mn^{2+}, Mn^{3+}, and Mn^{4+}) through XPS is usually performed through fitting with theoretically predicted peaks of individual ions,[34−36] satellite peak splitting and exchange peak splitting for the Mn 2p, 3s, and 3p peaks,[37] both of which are well documented for MnO_x systems,[34,37,38] such analyses are prone to large errors when applied to electrocatalytic studies where relative changes in the cation concentration in the mixed-valent state must be tracked.

In addition to the uncertainties in the relevant cation valent state, from a broader perspective, the underlying correlation between the cation valent state and the bifunctional property or lack thereof in certain electrocatalysts is not known. Therefore, understanding the fundamental origin of bifunctionality including the nature of reaction intermediates and their relation to the catalyst band structure is important not only for further enhancement of energy conversion efficiency but also for enabling the rational design of new multifunctional catalysts.

In this work, we report the first use of confocal near-infrared photoluminescence (NIR-PL) spectroscopy to probe the cation charge states of the active sites and the reaction intermediates. Using the results from the combined in situ electrical, spectroscopic, and gravimetric measurements on bifunctional Mn_2O_3 and nonbifunctional NiO_x, we show that electrocatalytic activities of an oxide crucially depend on the potential of formation of active defect sites relative to the potential of redox reaction and the local surface electrical resistivity. Bifunctionality in MnO_x arises as a result of the material's ability to undergo a facile switch in polarity from p-type to n-type during OER and reduction ORR, respectively, that gives rise to volcano-type changes in the resistance due to the formation of both high- and low-valent metal cation active sites. In contrast, most common oxides, such as NiO_x and Co_3O_4, show good catalytic activity for OER but not ORR, and are therefore nonbifunctional. This is due to a large increase in the sample resistance during ORR, which gates catalytic current, and is a result of unfavorable lattice defect energy.

EXPERIMENTS AND RESULTS

Electrochemical testing was performed on nominally undoped oxides of manganese (α-Mn_2O_3), cobalt (Co_3O_4), and nickel (NiO_x), whose activities were measured against the benchmarked activities of ruthenium dioxide (RuO_2) and platinum. X-ray diffraction (XRD) patterns of all oxide powders used here only showed the presence of a single phase, as shown in Figure S1 in the Supporting Information. Compositional analysis of both oxide phases using XPS through the established fitting procedure[35,36,38−41] (Figure S2 and Table S1) show that α-Mn_2O_3 oxide used here showed the presence of Mn^{4+} at a concentration of 10%, which is likely due to interstitial oxygen (O_i) or Mn cation deficiency, both of which are known to create acceptor-type states and native p-doping in Mn_2O_3, as reported in the literature.[42] Similarly, the composition of NiO_x was estimated to be $NiO_{2.1}$, as determined from the presence of Ni^{3+} defect states in Ni^{2+} lattice sites, resulting from the presence of excess lattice oxygen that gives rise to native p-doping of the material.[43]

Electrocatalytic OER and ORR activity of both oxides were benchmarked against the RuO_2 OER and Pt ORR activities using a glassy carbon (GC) rotating disk electrode (RDE) setup in O_2- and Ar-purged electrolytes of pH = 12 in a three-electrode setup. Electrocatalytic testing was also performed under static conditions on oxides dispersed on fluorine-doped tin oxide (FTO)-coated glass substrates to confirm the activity trends and to exclude any substrate effects. All electrodes were prepared without the use of any conductive carbon or fillers to avoid interference of carbon additives which are known to synergistically aid the ORR activity of certain oxides such as Co_3O_4.[12] Therefore, the reported current density values reflect the true intrinsic activity of the oxide whose area was estimated from the Brunauer−Emmett−Teller (BET) adsorption isotherm. All potentials referred in the text are with respect to the reversible hydrogen electrode (RHE) at pH = 12 unless otherwise noted. Figure 1A compares the linear-sweep voltammograms of Mn_2O_3, NiO_x, and Co_3O_4 electrodes on FTO substrates under static conditions. Figure 1B compares the Tafel polarization curves of the same oxides on GC RDE at a rotation speed of 1600 rpm using galvanostatic charging against the benchmarked OER and ORR activity of RuO_2 and polycrystalline Pt disk, respectively. The Tafel slope of 56 mV/decade of the Pt disk is in agreement with the 60 mV/decade slope reported for Pt/C and Pt nanoparticles in the literature.[44−48] Similarly, the Tafel slope of 100 mV/decade for OER activity of RuO_2 is in line with the value of ∼95 mV/decade reported for polycrystalline and single crystalline RuO_2.[49] Comparison shows that Co_3O_4 and NiO_x are good catalysts for OER but not for ORR, while Mn_2O_3 shows good activity for both OER and ORR, that is, it is bifunctional. This catalytic activity trend of various oxides on the GC electrode is similar to that observed with the FTO electrode. The cyclic voltammetry (CV) recorded for the Mn_2O_3 electrode in an Ar-purged electrolyte is shown in Figure 1C along with the labels for all the various potentials of peak currents. As can be seen, oxygen evolution was observed at potentials more positive than 1.9 V. The reduction of oxygen evolved during the anodic scan can be seen at potentials more negative than 0.7 V. Very little current is observed when the electrode is polarized in the cathodic direction alone.

To understand the origin of bifunctional activity of Mn_2O_3, we first measured changes in the electrical resistivity and the

https://dx.doi.org/10.1021/acs.jpcc.0c00714
J. Phys. Chem. C 2020, 124, 5286−5299

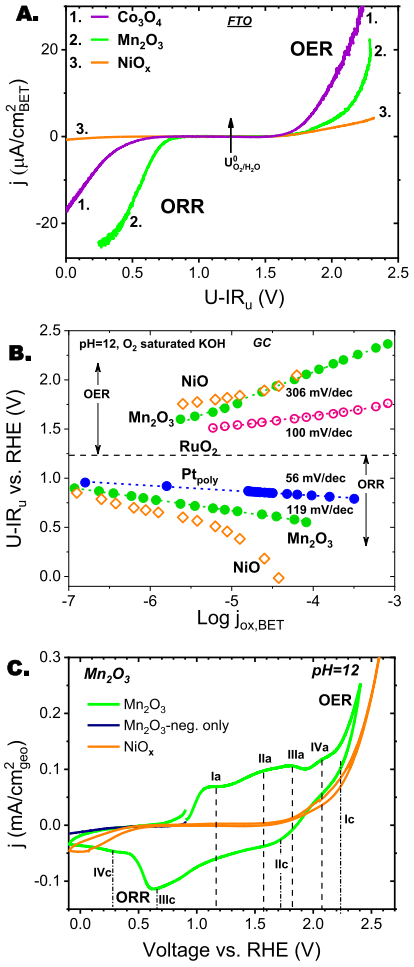

Figure 1. (A) Linear sweep voltammograms of several binary oxides on a FTO substrate; (B) Tafel polarization curves taken under galvanostatic conditions using GC RDE showing the catalytic activity of different oxides for OER and ORR in an O_2-purged electrolyte of pH = 12 at 1600 rpm; and (C) cyclic voltammogram of Mn_2O_3 and NiO_x on FTO electrodes obtained at a scan rate of 5 mV/s in an Ar-purged, pH = 12 aqueous electrolyte.

nature of majority charge carriers of the catalysts in situ during polarization through electrochemical impedance spectroscopy, as detailed in the Methods section. Nyquist plots of all oxide electrodes showed two semicircles (Figure 2A) and were fitted with an equivalent circuit model, $R_S(R_BC_B)(R_{CT}C_{DL}W)F_D$, shown in the inset of Figure 2A, that accounts for: (i) solution resistance, R_S; (ii) bulk electrode resistance, R_B, in parallel with the bulk capacitance, C_B, to account for any changes in the bulk of the semiconductor because of ion insertion; (iii) oxide/electrolyte interface with charge transfer resistance and surface electronic resistance, R_{CT}, and Warburg impedance, W, in parallel with the double layer capacitance, C_{DL}; and (iv) a finite diffusion element, F_D, in addition to W to account for the low-frequency diffusion tail. In this model, both the charge transfer resistance and surface electronic resistance is represented by R_{CT} because active sites that enable binding of intermediates through changes in the metal valent states also lead to the increase in the electrical conductivity of the oxide.[50] This assertion is discussed in detail later. Figure S3 in the Supporting Information shows the accuracy of the model used for the fitting analysis of data generated from impedance measurements for a wide range of polarization potentials. Table S2 in the Supporting Information provides the example of values estimated for various elements extracted from the fitting analysis for Mn_2O_3 in the pH = 12 electrolyte. The bulk resistance (R_B) along with R_S showed no significant change in its value over the entire potential range, as seen in Figure 2A, while R_{CT} showed significant changes with polarization potential. This indicates that electrochemical processes are likely restricted to the surface.

The total electrical resistance (R_{total}), as given by the sum of R_{CT}, R_B, and R_S, of various oxides polarized between OER and ORR potentials showed marked changes in the electrical resistivity on the order of 10^2 to 10^4, as shown in Figure 2B–D Bifunctional Mn_2O_3 electrode showed a volcano-type resistance plot with a large increase in resistance at intermediate potentials between OER and ORR potentials, while it showed low resistance (metallic conductivity) at potentials that coincide with potential regions of high electrocatalytic OER and ORR currents. This indicates that catalytic activity is governed by the surface electrical conductivity and charge transfer resistance. A similar pattern of resistance change was also observed in slightly acidic electrolytes, which is shown for Mn_2O_3 for the pH = 4 electrolyte in Figure 2B. The resistance of Mn_2O_3 decreased slightly during polarization in the forward scan from open-circuit potential (OCP) up to OER potential, but the conductivity was essentially metallic (~80 Ω). However, a progressive increase in the resistance, which is similar to that observed for the pH = 12 electrolyte but with a higher magnitude of resistance change, was measured during the reverse scan from OER to ORR. The maximum in resistance occurred at 0.1 V (~3 kΩ) and 0.65 V (~22 kΩ) in pH = 12 and pH = 4 electrolytes, respectively, with respect to the RHE. Given that resistivity is lower in basic electrolytes (note the magnified scale) than in acidic electrolytes, this indicates that the nature of the species responsible for resistance changes depends on the H^+ concentration in the medium. In contrast to bifunctional Mn_2O_3, the resistance changes in nonbifunctional oxides, namely, Co_3O_4 and NiO_x, showed that they undergo a metal-to-insulator transition between the OER and ORR potential scans. Both Co_3O_4 and NiO_x showed increased conductivity during the potential scan from OCP to OER. This potential region of high electrical conductivity coincides with a region of high OER activity. Thus, metallic conductivity aids in catalyzing OER, while the formation of an insulating phase at negative polarizations gates the electrocatalytic ORR current. For all oxides tested, the measured resistance values at a given potential were nearly similar during forward and backward potential scans, as seen, for instance, from the resistance values measured at OCP and at that same potential during the reverse ORR scan, which indicates that the processes inducing resistance changes, likely involving ion insertion, are reversible.

In addition to resistance changes, Mott–Schottky (M–S) measurements were performed at a fixed frequency of 1000 Hz both at OCP and after electrochemical prepolarization at anodic (2.1 V, OER region) and cathodic (0 V, ORR region) potentials for 10–30 min to determine the sign and density of majority charge carriers. According to the results shown in Figure 3, Mn_2O_3, in addition to the resistance changes, undergoes a switch in the polarity of majority charge carriers from p-type during OER to n-type at ORR potentials. The electrode showed a p-type behavior at OCP in both basic and acidic (inset of Figures 3A, and S4, respectively) electrolytes that are consistent with native p-type doping because of the

https://dx.doi.org/10.1021/acs.jpcc.0c00714
J. Phys. Chem. C 2020, 124, 5286–5299

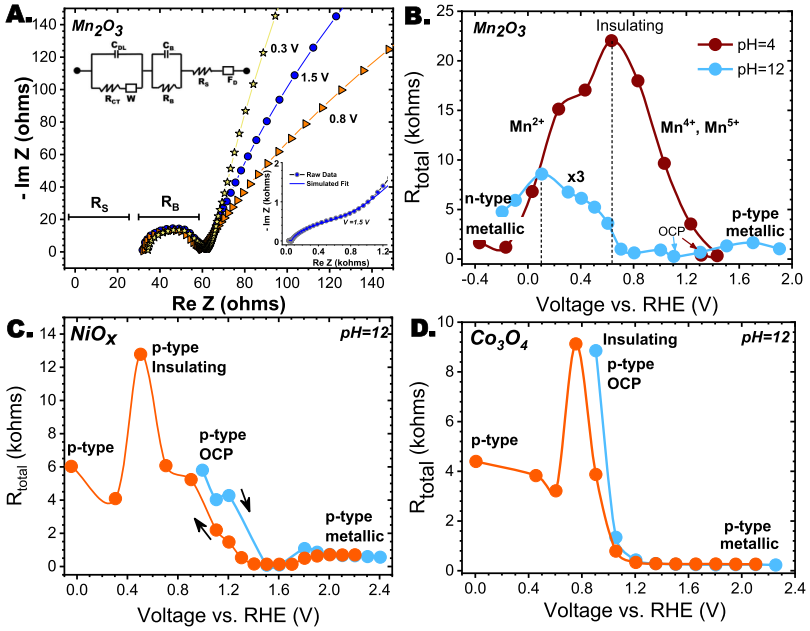

Figure 2. (A) Nyquist plot of the Mn_2O_3 electrode at several polarization potentials in a pH = 12 electrolyte. The inset shows the same plot and simulated curve over a wider frequency range obtained for 1.5 V polarization potential. Also, shown is the schematic of the equivalent circuit used for simulation; (B,C) changes in the total electrical resistance, which is the sum of charge transfer resistance, R_{CT}, bulk resistance, R_B, and solution resistance, R_S, estimated from impedance analysis of bifunctional (α-Mn_2O_3) and nonbifunctional (Co_3O_4, and NiO_x) oxides.

Mn^{4+} cations, as observed from XPS results. The flat band potential, U_{FB}, occurred at ~0.62 V versus RHE or −4.82 eV with respect to the vacuum energy scale.[51] While exhibiting the same p-type behavior, the U_{FB} shifts to 1.4 V after the electrode was anodically prepolarized. In contrast, the polarity changes to n-type with a shift in the U_{FB} to 0.6 V after cathodic polarization. This switch in the polarity of majority charge carriers from p-type to n-type between OER and ORR scan potentials was observed in all electrolytes of pH values between 4 and 13. The results obtained for pH = 4 electrolyte is shown in Figure S4 in the Supporting Information. This change in the conductivity between p-type to n-type during ORR scan would explain the volcano-type resistance trend and is likely due to the formation of an insulating surface phase because of passivation of native hole dopants at the surface by injected electrons. In contrast to Mn_2O_3, no such change in the electrical polarity from p-type to n-type was observed in nonbifunctional oxides (Co_3O_4, and NiO_x), as seen from Figure 3B,C. Both oxides showed only p-type behavior under different prepolarization conditions. Therefore, it can be concluded that the bifunctional Mn_2O_3 electrode has the ability to switch electrical polarity between p-type that enables efficient h^+ transfer for oxidative processes (OER) to n-type that enables e^- transfer for efficient reductive processes (ORR). In contrast, nonbifunctional oxides (Co_3O_4 and NiO_x) show unipolar conductivity, that is, either n-type or p-type but not both, and are therefore more efficient for either the OER or ORR process but not both and as a result are irreversible toward the oxygen reaction. Their inability to switch polarity results instead in the formation of an insulating surface phase during one of the oxygen reaction processes that gate the catalytic current.

It was observed that changes in the electrical polarity and the density of majority carriers with anodic and cathodic prepolarization were dependent on the electrolyte pH. The density of uncompensated majority charge carriers was estimated from the slope of the M−S plot measured at varying electrolyte pH and is shown in Figure S5. Here, the hole carrier density is represented as a positive value, while electron density is denoted as a negative value. Given the particulate nature of the electrode, the value of the estimated charge carrier density is only approximate. Nevertheless, values measured in electrolytes of different pH can be qualitatively compared because the geometric area and weight of the electrodes were nearly similar for measurements in different electrolytes. Several interesting trends were observed: (i) a switch in conductivity from p-type to n-type was observed at all pH values of the electrolyte with cathodic prepolarization; (ii) the Mn_2O_3 electrode exhibited a greater p-type character, as seen from the higher hole carrier density under basic conditions compared to that in acidic conditions. The hole carrier concentration increased with pH both at OCP and after positive polarization; and (iii) the n-type character was dominant under acidic conditions. This was seen from the increasing value of electron carrier density, measured after negative prepolarization, with decreasing electrolyte pH. The smaller n-type character seen in the basic electrolyte is also reflected in the higher resistance value of ~2 kΩ (semiconducting) of the electrode compared to the value of ~150 Ω in the acidic electrolyte at 0 V polarization.

More in-depth characterization was performed using Mn_2O_3 and NiO_x as prototypical bifunctional and nonfunctional oxides, respectively, to probe the nature of reaction intermediates responsible for the origin of resistance and polarity changes.

First, it was confirmed that the observed changes in the resistance and electrical polarity is due to irreversible compositional changes occurring during polarization through XRD measurements (Figure S6A) of the emersed Mn_2O_3 electrode after polarization at various potentials. Prior Raman[52] and XAS[31] studies indicate that electrodeposited MnO_x undergoes an irreversible phase transformation to Mn_3O_4 at the ORR potential or at potentials more negative

https://dx.doi.org/10.1021/acs.jpcc.0c00714
J. Phys. Chem. C 2020, 124, 5286−5299

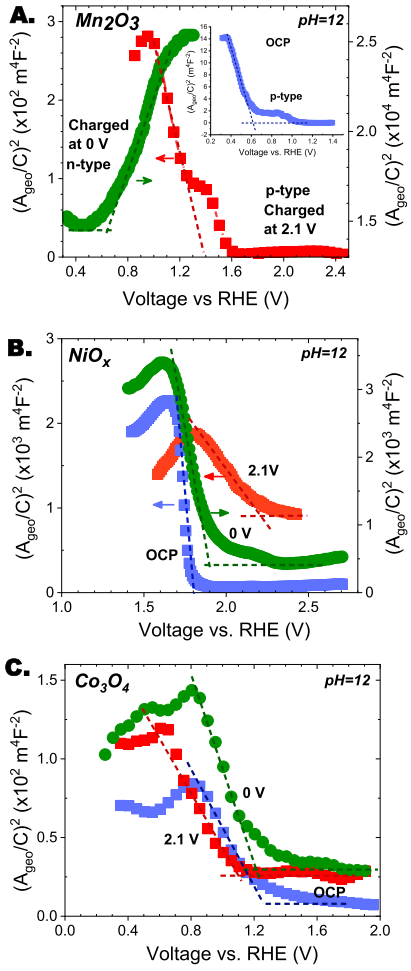

Figure 3. M−S plots of oxides at OCP and after charging at 2.1 and 0 V polarization. Mn_2O_3 (A) shows a polarity switch from p-type and n-type between the OER and ORR scan. On the other hand, NiO_x (B) and Co_3O_4 (C) show no change in the electrical polarity between OER and ORR scan. Both show only p-type behavior.

than −0.6 V versus SHE. Results here show that crystalline Mn_2O_3 prepared using the solid−state reaction technique is stable against irreversible compositional changes. No bulk phase transformation could be detected through XRD after the electrode was polarized at both oxidizing (2.3 V) and reducing (0.3 V) potentials for 20 min in the pH = 12 electrolyte. More surface-sensitive Raman measurements (Figure S6B) were also performed on emersed electrodes after polarization at various potentials. The Mn_2O_3 electrode showed a strong vibrational peak at 651.7 cm^{-1} and weak peaks at 366 and 309 cm^{-1}, all of which are characteristic of Mn−O stretches of bixbyite α-Mn_2O_3,[53] while a slight reversible shift of the 651.7 cm^{-1} peak of ∼1.2 cm^{-1} to the higher (lower) wavenumber with positive (negative) polarization was observed, which is consistent with the decrease in the bond length, resulting from the oxidation (reduction) of the metal cation site with polarization.[54,55] No formation of Mn_3O_4 was observed, which has the characteristic Raman peak at 659 cm^{-1},[52] and is consistent with XRD results. The only region of considerable shift was during polarization at 0.6 V that corresponded to ORR. At this potential, the dominant peak at 651.7 cm^{-1} disappeared and two new peaks at 316 and 410 cm^{-1} appeared, the latter of which is characteristic of $Mn(OH)_2$.[56] Further polarization recovered the characteristic bixbyite peak at 650 cm^{-1}.

To determine the nature of various ion insertion processes that lead to the formation of reaction intermediates that give rise to changes in the surface resistance, time-dependent changes of the Mn_2O_3 electrode mass was measured by electrochemical quartz crystal microbalance (EQCM). Figure 4A shows the mass change, defined as the change in the mass of the electrode with respect to the mass recorded at OCP per unit geometric area, of the Mn_2O_3 electrode occurring during potential cycling between OER and ORR steps recorded at a scan rate of 5 mV/s in the pH = 12 electrolyte. The profile shows several regions with distinct features that are marked with letters A through J. First, the profile shows that there is no loss in the total mass but rather a small gain at the end of the CV cycle. This indicates that the contribution of corrosion to the measured mass change was negligible within the testing period (typically two cycles).[57] In the region A−B, which corresponded to the potential range of 0.9−1.9 V that precedes the OER step, the electrode showed a continuous increase in mass, which is consistent with the insertion of OH^- into the lattice sites. In the same potential range, CV (Figure 1C) showed distinct peaks, Ia, IIa, and IIIa, at 1.1, 1.55, and 1.8 V, respectively, which indicates that such peaks correspond to OH^--induced formation of intermediates that also give rise to changes in resistivity.[58] In addition, the EQCM profile indicates the occurrence of secondary processes that are also of interest: (i) a mass loss between 2.0 and 2.2 V during O_2 evolution (region B−C) at a potential greater than 1.9 V; (ii) a significant mass increase (46% of total increase) at potentials higher than 2.2 V (region C−D) that continues even upon potential reversal, which points to an inserting species that is neutral and is not associated with e^- exchange (likely H_2O); (iii) a large mass loss (∼75% of total loss) occurs between 1.25 and 0.9 V (region G−H). Wu et al.[57] observed a similar mass loss in MnO_2, which they showed through charge-to-mass calculations to be due to the loss of H_2O. It is likely that this may be the reason for mass loss in Mn_2O_3 as well; and (iv) a small mass gain (region H−I) at potentials more negative than 0.9 V. Because Raman measurements show the formation of $Mn(OH)_2$ at 0.6 V, the observed mass gain is attributed to the formation of $Mn(OH)_2$.

While the above results confirm the formation of ion-induced intermediates, their effect on resistivity and catalytic activity can only be understood if the charged state of these intermediates (defects) is known. While prior X-ray absorption studies have conclusively shown that the average oxidation state of Mn increases to +3.4 during OER and decreases to +2.4 during ORR,[30,31] the exact nature and the relative concentration of individual metal valence states in the mixed-valent catalyst could not be determined. We recently reported through studies on several different oxides and chalcogenides[41,59,60] the first use of confocal NIR-PL as a technique for studying various cationic defects of various oxidation states under in-operando Li^+ insertion process conditions. Here, we demonstrate its first application to the ex situ study of the electrocatalyst under electrochemical conditions.

The spectral range of radiative emissions seen in metal oxides is shown in Figure S7.[61] Electronic transitions between the ligand (L) and metal charge transfer and metal to conduction band (CB) transitions frequently occur in the ultraviolet (UV) spectral range. The d−d transitions are usually in the visible region, and defect-related emissions, both cationic and anionic, are in the visible to NIR spectral region.[41] In the case of MnO_x, the characteristic emission from electronic transitions of

https://dx.doi.org/10.1021/acs.jpcc.0c00714
J. Phys. Chem. C 2020, 124, 5286−5299

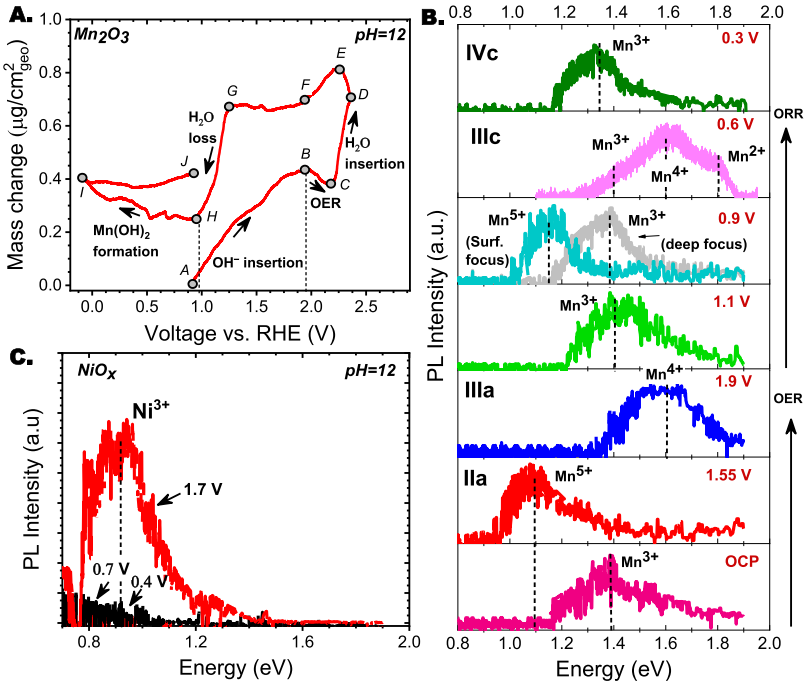

Figure 4. (A) Mass change of a Mn_2O_3 electrode during CV; (B) ex situ NIR PL spectra of the emersed Mn_2O_3 electrode after polarization in a pH = 12 electrolyte at various voltages. The observed surface shifts in the emission peak reflects the changes in the oxidation state of the Mn atom during polarization; (C) changes in the intensity of NIR emission of NiO_x after polarization in the pH = 12 electrolyte at various potentials. The formation of Ni^{3+} defect states is observed at positive polarization. The complete quenching of the 0.9 eV emission is due to passivation of Ni^{3+} during negative polarization, which results in the formation of an insulating phase.

various cationic defects (Mn^{2+}–Mn^{6+}) occur in the 0.9–1.9 eV spectral range: $^4T_{1g} \rightarrow {}^6A_{1g}$ of Mn^{2+} at 1.8 eV, $^3T_{1g} \rightarrow {}^5E_{1g}$ of Mn^{3+} at 1.3 eV, $^2E_{1g} \rightarrow {}^4A_2$ of Mn^{4+} at 1.6 eV, and $^3T_2 \rightarrow {}^3A_2$ of Mn^{5+} at 1.1 eV.[62−67] The energies of characteristic emissions were confirmed in the present study through measurements with reference mineral/oxide powders and XPS measurements, and are shown in Figure S8. Because the characteristic photoluminescence (PL) emission of different Mn oxidation states occur at distinct energies, resolution of the contributions from individual Mn cations is very straightforward compared to X-ray absorption or emission analysis. Therefore, the technique is uniquely suited for studying electrocatalytic intermediates.

The surface sensitivity of the PL technique using common setups depends both on the wavelength of light and diffusion of photoexcited carriers. For an excitation wavelength of 633 nm, the penetration depth spans tens to hundreds of nanometers in our system. However, the use of the confocal microscope setup enables one to screen signal coming from out-of-focus bulk planes and achieve true surface sensitivity. Therefore, depth-dependent changes in the confocal PL spectrum allow one to distinguish bulk versus surface intermediates without sample destruction.

Figure 4B shows the ex situ NIR emission spectrum from the Mn_2O_3 electrode polarized at various potentials corresponding to the redox peaks observed in the CV (Figure 1C) in the pH = 12 electrolyte. All spectra were recorded using a 633 nm laser light focused on the sample surface through a confocal microscope. While the spectra are slightly noisy because of the use of a very low laser power of 1.7 mW to avoid spot damage due to localized laser heating, the ratio of peak signal to background was high (10^2). At OCP, the emersed electrode shows only the characteristic emission of Mn^{3+} at 1.4 eV. Positive polarization at 1.55 V (anodic peak IIa) leads to the shift in the emission peak to a lower energy of 1.1 eV that is characteristic of Mn^{5+}. Further polarization at 1.9 V (peak IIIa) results in the disappearance of Mn^{5+}-related emission and an appearance of the Mn^{4+}-related signal. While this observation of an increase in the Mn oxidation state with anodic polarization confirms prior results, we report here the first observation of Mn^{5+} formation during water oxidation, which has been predicted by theoretical calculations[29] but has not been observed experimentally by other spectroscopic techniques in both natural and synthetic manganese oxide catalysts.[68,69]

During the cathodic potential scan at 1.1 V polarization, the electrode only shows a dominant peak of Mn^{3+} at 1.4 eV, indicating that the sample retains the crystal structure of Mn_2O_3 after the end of the positive cycling, which was confirmed from Raman and XRD measurements discussed earlier. At 0.9 V, the emission peak shifts to a lower energy of ~1.1 eV that indicates the formation of Mn^{5+}. During ORR at a potential of 0.6 V (CV peak IIIc), the sample exhibits mixed oxidation states of Mn^{2+}, Mn^{3+}, and Mn^{4+} but with an increased contribution from Mn^{2+}. This formation of the lower valent metal cation (Mn^{2+}) at ORR potential is a striking observation, which is shown later to be the key difference that differentiates bifunctional and non-bifunctional electrocatalysts. There is also a complete disappearance of Mn^{5+} at negative potentials. After polarization at 0.3 V (CV peak IVc), only emission from Mn^{3+} is observed.

Emission spectra taken at varying focus depths indicated that all observed changes in the Mn oxidation state were restricted to the surface. For example, Figure 4B shows the spectrum of the Mn_2O_3 electrode at 0.9 V at two different focus depths. The spectrum from the surface ("surf. focus") shows a strong peak from Mn^{5+} cations, while the spectrum from the same spot but

https://dx.doi.org/10.1021/acs.jpcc.0c00714
J. Phys. Chem. C 2020, 124, 5286−5299

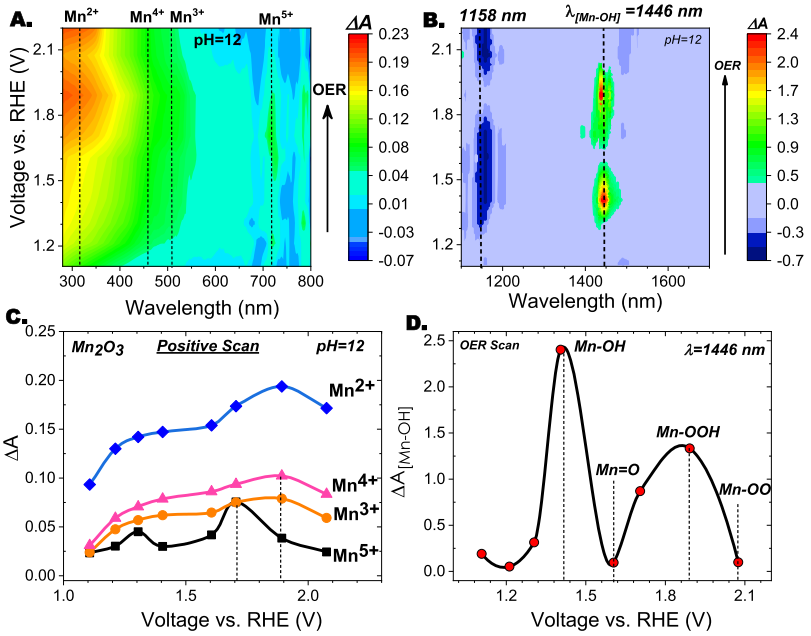

Figure 5. In situ changes in the difference absorbance of Mn_2O_3 in the UV−vis (A,C) and NIR (B,D) during potential scan from OCP to OER, respectively, in pH = 12 electrolyte; (C) changes in the difference absorbance of the Mn_2O_3 electrode at 320, 510, 460, and 720 nm corresponding to the Mn oxidation state of +2, +3, +4, and +5, respectively, during positive potential scan from OCP to 2.2 V; (D) changes in the $\Delta A_{[Mn-OH]}$ vs various applied potentials during positive scan.

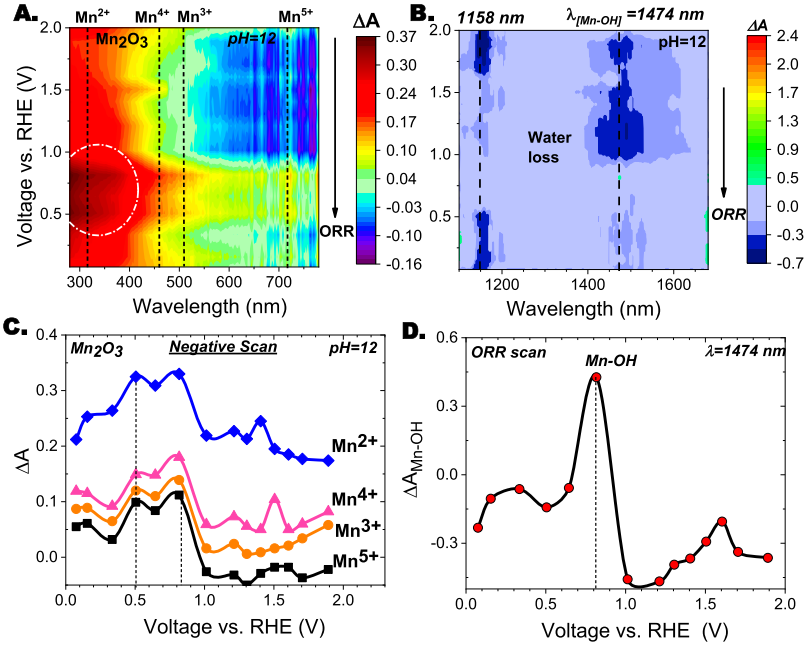

Figure 6. In situ changes in the difference absorbance of Mn_2O_3 in the UV−vis (A,C) and NIR (B,D) during reverse potential scan from OER to ORR, respectively, in the pH = 12 electrolyte; (C) changes in the difference absorbance of the Mn_2O_3 electrode at 320, 510, 460, and 720 nm corresponding to the Mn oxidation state of +2, +3, +4, and +5, respectively, during reverse potential scan; and (D) changes in the $\Delta A_{[Mn-OH]}$ vs various applied potentials during reverse scan.

focused to deeper sample depth ("deep focus") showed only the signal from Mn^{3+} lattice ions. Unlike other MnO_x phases such as δ- or α-MnO_2 that have layered or tunneled MnO_6 octahedral arrangements with large void spaces that enables ion insertion into the bulk lattice, Mn_2O_3 has a closed three-dimensional arrangement with no void space. Therefore, it is likely that OH^- insertion is restricted to the surface in Mn_2O_3.

In contrast, the results of emission measurements on a nonbifunctional NiO_x electrode at varying potentials (Figure 4C) showed the formation of the higher-valent cation (Ni^{3+}) during OER scan but no formation of the lower-valent cation (Ni^+) could be observed during cathodic polarization. The pristine NiO_x electrode shows broad but intense emission centered at 0.9 eV that is characteristic of Ni^{3+} ions, as shown in an earlier study.[41] Immersion in the pH = 12 electrolyte at OCP quenches this NIR emission intensity. Positive polarization at 1.7 V leads to an increase in the Ni^{3+} emission peak that is consistent with prior results.[70] This emission peak,

https://dx.doi.org/10.1021/acs.jpcc.0c00714
J. Phys. Chem. C 2020, 124, 5286−5299

however, is quenched completely at all potentials negative of 0.7 V. No formation of Ni^{+}-related donor defect emission, which has a characteristic peak emission at ~0.7 eV,[41] could be observed even when polarized down to 0 V. The absence of donor-type defect state (Ni^{+}) formation in nonbifunctional NiO_x is in striking contrast to bifunctional Mn_2O_3 that shows the formation of a donor-type Mn^{2+} at a relatively low overpotential. This absence of a lower oxidation defect state is the key property that distinguishes bifunctional oxides from nonbifunctional oxides with regard to ORR activity.

The NIR-PL results showing changes in the oxidation states were independently confirmed with in situ absorbance measurements (Figures 5 and 6). While PL is a surface-sensitive probe, absorption measurements probe the bulk of the film. Because PL results also show that changes in valence states are restricted to the surface, we use the bulk-sensitive probe to observe changes at the surface. All absorbance measurements on Mn_2O_3 and NiO_x electrodes were performed in situ in the diffuse reflectance mode during electrochemical polarization in pH = 12 electrolytes from the UV to NIR spectral range. The changes in the UV to visible spectral range contain excitation transitions of the various oxidation states of Mn atoms are as follows: ${}^6A_{1g} \rightarrow {}^4T_{1g}$ of Mn^{2+} at ~320 nm,[65,71] ${}^5E_{1g} \rightarrow {}^5T_{2g}$ of Mn^{3+} at 510 nm,[72] ${}^4A_2 \rightarrow {}^4T_{2g}$ of Mn^{4+} at 460 nm, and ${}^3A_2 \rightarrow {}^3T_2$ (${}^3F$) of Mn^{5+} at 720 nm.[63,67] The NIR spectral range contains a combination of stretching and deformation vibrations of hydrogen-bonded water molecules to the surface OH groups at 1158 nm,[73−75] and the first overtone stretching vibration of Mn−OH related groups, [Mn−OH], at 1446 nm.[73,74]

The difference absorbance (ΔA) spectra, defined as the absorbance relative to the value measured at OCP, of the Mn_2O_3 electrode during polarization from OCP to 2.2 V in pH = 12 electrolyte in the UV−vis and NIR spectral ranges are shown in Figure 5A,B, respectively. The changes are perhaps best seen in the ΔA versus voltage plot shown in Figure 5C,D. Consistent with the observed CV peaks and results of NIR-PL measurements, in situ absorbance results show increased intensity of Mn^{4+} at 1.1−1.4 V (CV peak Ia), Mn^{5+} at 1.55 V (peak IIa), Mn^{4+} again at 1.9 V (peak IIIa), and Mn^{5+} at 2.1 V (peak IVa). A striking feature is the observation of cyclic changes in the intensity of $\Delta A_{[Mn-OH]}$: two positive maxima at 1.4 and 1.9 V, indicating an increase in Mn−OH vibration strength and two minima (zero ΔA) at 1.6 and 2.1 V, respectively. These potentials coincide with the three anodic peak potentials (IIa, IIIa, and IVa) seen in the CV at 1.55, 1.8, and 2.1 V, respectively, which suggests that changes in the $\Delta A_{[Mn-OH]}$ reflect the formation of various intermediates of OER. Oxygen evolution is known to proceed as a series of one-electron intermediates starting from the formation of $-OH^{-}$ and leads to the sequential formation of $=O^{2-}$, $-OOH^{-}$, and $-OO^{2-}$, that also results in the change in the metal cation valence state.[24,49] Therefore, one would expect an increase in $\Delta A_{[Mn-OH]}$ with the formation of $Mn^{4+}-OH^{-}$ and $Mn^{4+}-OOH^{-}$ intermediates and a decrease in the $\Delta A_{[Mn-OH]}$ signal as a result of $Mn^{5+}=O^{2-}$ and $Mn^{5+}-OO^{2-}$ coverage. The NIR changes confirm this trend. It is emphasized here that NIR signals do not provide the spectroscopic signature of these intermediates. Rather, their formation is surmised through the potential-dependent changes in the Mn−OH vibrational intensity.

From the observed changes in the metal valent states and type of oxygen intermediates, the following OER steps are proposed that is fully consistent with theoretical predictions of Fernando et al.[29] and Su et al.[24]

OER Step-I: Localization of a hole (h^{+}) at the Mn^{3+} lattice site to form the Mn^{4+} site (polaron) active site.

$$Mn^{3+} + h^{+} \rightarrow Mn^{4+} \qquad U = 1.1-1.4\ V \tag{1a}$$

OER Step-II: A high-valent Mn^{4+} site (polaron) site serving as the active sites for ion adsorption.

$$Mn^{4+} + OH^{-} \rightarrow Mn^{4+} - OH^{-} \qquad U = 1.1-1.4\ V \tag{1b}$$

$$Mn^{4+} - OH^{-} + OH^{-} \rightarrow Mn^{5+} - O^{2-} + e^{-} + H_2O \qquad U = \sim 1.55\ V \tag{2}$$

$$Mn^{5+} - O^{2-} + OH^{-} \rightarrow Mn^{4+}-OOH^{-} + e^{-} \qquad U = \sim 1.9\ V \tag{3}$$

$$Mn^{4+}-OOH^{-} + OH^{-} \rightarrow Mn^{5+}-OO^{2-} + e^{-} + H_2O \qquad U = \sim 2.1\ V \tag{4a}$$

$$Mn^{5+}-OO^{2-} \rightarrow Mn^{3+} + O_2 \quad \text{chemical step} \tag{4b}$$

This mechanistic pathway for OER is shown schematically in Figure 7A.

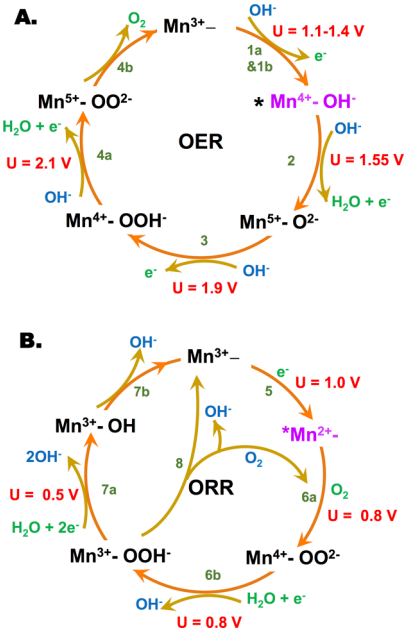

Figure 7. Schematic showing the mechanistic pathway for OER (A) and ORR (B) on the Mn_2O_3 surface. * here represents the active Mn cation site. The potential (U) of formation of various intermediates from the CV, NIR-PL, and absorbance results are also indicated.

Absorbance changes during cathodic polarization (Figure 6, ORR scan) show that no significant changes to the Mn valent states occur until 0.8 V (onset of peak IIIc), which is the onset of ORR. At this voltage, Mn_2O_3 shows the strongest increase in the Mn^{2+} signal along with smaller increases in the Mn^{3+} and Mn^{4+} signals. Such a mixed-valent state was also seen in the NIR-PL spectrum at 0.6 V. Because the ORR process does not initiate until the formation of Mn^{2+}, it is concluded that Mn^{2+} is the catalytic site for the ORR process.

https://dx.doi.org/10.1021/acs.jpcc.0c00714
J. Phys. Chem. C 2020, 124, 5286−5299

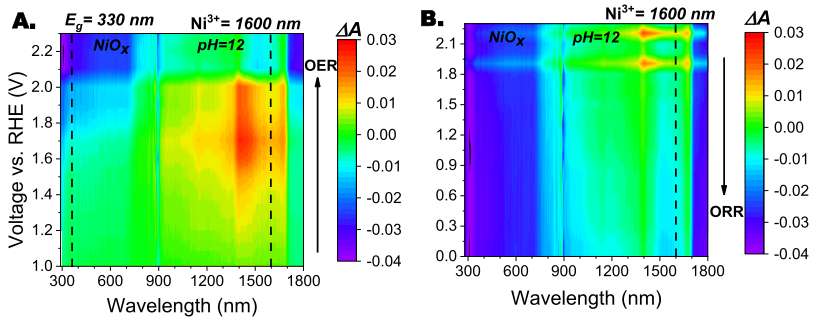

Figure 8. Changes in the difference absorbance in the UV−vis spectral region of the NiO_x electrode during potential scan to OER (A) and ORR (B) in the pH = 12 electrolyte.

In-depth microkinetic studies on Mn_2O_3 by Mao et al.[76] show that ORR proceeds through a four-electron direct pathway involving two sequential steps consisting of the reduction of adsorbed OO^{2-} to the peroxide ion, $-OOH^-$, followed by a two-electron reduction of $-OOH^-$ to OH^-. They also noted that Mn_2O_3 is an excellent catalyst for chemical disproportionation of $-OOH^-$ to molecular O_2 that further undergoes the above $4e^-$ reduction pathway.[15,76,77] The measured charged states of Mn cations (Mn^{2+}, Mn^{3+}, and Mn^{4+}) at 0.8 V ORR potential in the present study are consistent with their mechanistic pathway given below:

ORR-Step-I: Localization of electron at the Mn^{3+} lattice site to form the Mn^{2+} site (polaron) active site.

$$Mn^{3+} + e^- \rightarrow Mn^{2+}\ (\text{active site}) \qquad U = \sim 1.0\ \text{V} \tag{5}$$

ORR-Step-II: Adsorption of O_2 and its further reduction at the Mn^{2+} active site.

$$Mn^{2+} + O_2 \rightarrow Mn^{4+}{-}OO^{2-} \qquad U = 0.8\ \text{V} \tag{6a}$$

$$Mn^{4+}{-}OO^{2-} + H_2O + e^- \rightarrow Mn^{3+}{-}OOH^- + OH^- \qquad U = 0.8\ \text{V} \tag{6b}$$

$$Mn^{3+}{-}OOH^- + H_2O + 2e^- \rightarrow Mn^{3+}{-}OH^- + 2OH^- \qquad U = 0.3{-}0.5\ \text{V} \tag{7a}$$

$$Mn^{3+}{-}OH^- \rightarrow Mn^{3+} + OH^- \qquad U = 0.3{-}0.5\ \text{V} \tag{7b}$$

Chemical disproportionation

$$2Mn^{3+}{-}OOH^- \rightarrow 2Mn^{3+} + O_2 + 2OH^- \tag{8}$$

The observed mixed valent state of the catalyst at 0.8 V is consistent with the charge states of ORR intermediates, namely, $Mn^{4+}{-}OO^{2-}$ and $Mn^{3+}{-}OOH^-$ at the Mn^{2+} cation site that serves as the active site for ORR. A decrease in the Mn^{2+} signal at potentials less than 0.5 V together with an increase in the Mn^{3+} signal seen with NIR-PL provides support that Reactions 7a and 7b occur between 0.3 and 0.5 V (CV peak IVc).

Some secondary processes also occur that are evident in the absorbance changes that can be correlated to the changes seen in EQCM results. The intensity of $\Delta A_{[Mn-OH]}$ is red-shifted from 1446 nm (seen during positive bias) to 1474 nm with negative values at all voltages positive of 0.8 V during the cathodic scan. Both the wavelengths of stretching vibration of surface −OH bonds depend sensitively on the level of hydration. At these potentials, EQCM results indicate the insertion of water into the lattice sites. The absorbance switches to a positive value at 0.8 V that coincides with the potential at which EQCM results show a mass loss that is also likely due to the loss of H_2O. Theoretical calculations of Rossmeisl and coworkers[24] predict that the ORR is triggered with the loss in lattice water, which supports both of these observations. The loss of lattice water would lead to the recovery of Mn−OH stretching vibration (positive ΔA values). A small increase in Mn^{5+} is observed at 0.9 V (NIR-PL, UV−vis) but that disappears at lower polarization potential. This charge state is a consequence of adsorption of molecular O_2 as OO^{2-} at the Mn^{3+} site and may occur in parallel with O_2 adsorption at the Mn^{2+} site. However, given that this signal is much smaller than the signal of Mn^{2+} and Mn^{4+}, we conclude Mn^{3+} is not the active site for the ORR process.

Similar absorption measurements in the pH = 4 electrolyte (Figure S9A,B) show the increased formation of Mn^{2+} in the lattice both at potentials more positive than 1.6 V and at potentials less negative than 0.9 V during the negative scan, indicating a more facile formation of Mn^{2+} under low pH conditions.

For comparison, spectroscopic measurements were also conducted on a nonbifunctional catalyst of the NiO_x electrode in the pH = 12 electrolyte, and is shown in Figure 8A,B. During positive potential scanning (Figure 8A), the electrode shows an increase in the defect-related Ni^{3+} absorbance in the NIR spectral region, indicating an increase in the formation of Ni^{3+} at the potential leading up to OER, which is consistent with the results of NIR-PL measurements. The concentration of this Ni^{3+} defect is essentially quenched during the negative scan at all potentials more negative than 0.7 V, which agrees with the NIR-PL results as well. This quenching of acceptor defects results in the formation of an insulating phase. No formation of donor-type defect states was observed in NiO_x even at high cathodic polarization.

DISCUSSION

The combined electrical, gravimetric, and spectroscopic results show several differences between bifunctional and nonbifunctional catalysts. Here, we show the underlying correlation between electrical conductivity, cation valent state, and ion-insertion processes between the two types of semiconducting bifunctional and nonbifunctional oxides.

The two main observations distinguishing bifunctionality and a nonbifunctional catalyst are as follows: (i) the formation of both high-valent (Mn^{4+}) and low-valent (Mn^{2+}) cation charge states in Mn_2O_3 that serve as active sites for OER and ORR, respectively, while only a high-valent cation (Ni^{3+}) is

https://dx.doi.org/10.1021/acs.jpcc.0c00714
J. Phys. Chem. C 2020, 124, 5286−5299

observed in NiO_x during OER and no formation of low-valent Ni^+ was observed; and (ii) bifunctional oxides show a switch in the electrical polarity from p-type during OER to n-type during ORR with a volcano-type resistance change, while nonbifunctional catalysts (NiO_x and Co_3O_4) show no polarity switch and exhibit an insulating state during ORR. To understand the correlation between the two, we consider the band lineup of these oxides. The band diagrams of various oxides were constructed using the measured values of band gaps from optical measurements (Figure S10) and flat band potentials estimated at OCP in the pH = 12 electrolyte (Figure 3) and are shown schematically in Figure 9A with respect to the

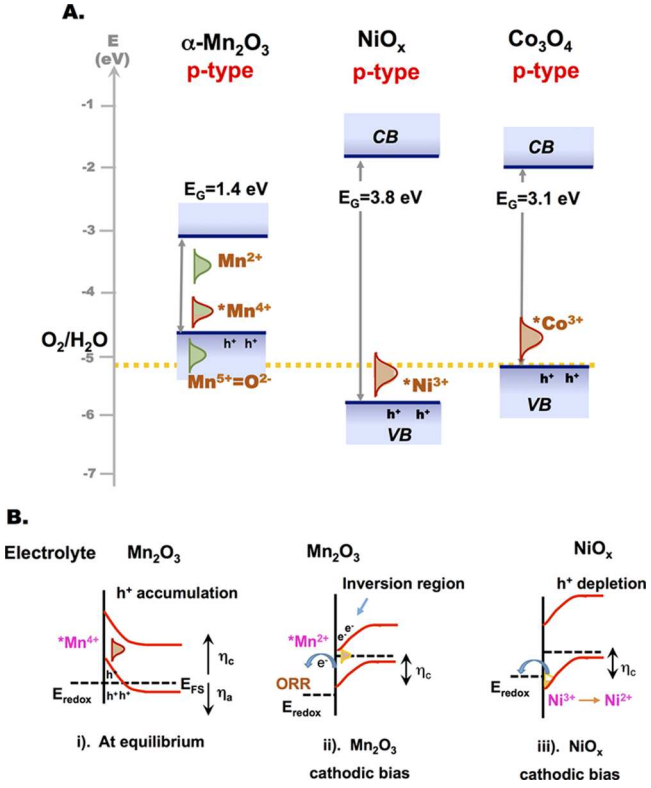

Figure 9. (A) Schematic of the energy band diagrams of Mn_2O_3, NiO_x, and Co_3O_4 showing the native cation (dopant) states (marked with *) and cation states formed during electrochemical polarization in the pH = 12 electrolyte. Band bending due to polarization is not shown for clarity; and (B) schematic illustrating the nature of band bending in a p-type semiconductor (e.g., Mn_2O_3 and NiO_x) at equilibrium and during cathodic polarization during ORR. In small band gap Mn_2O_3, polarization leads to the formation of an inversion region on the surface, while in the large band gap NiO_x, it leads to the formation of the hole depletion (insulating) region.

electrolyte. Also, shown in the figure are the approximate positions of both native metal cation dopant states (shown with *), as well as those intermediate metal cations that are generated during electrochemical polarization. Their formation potentials were obtained from CV, PL, and optical absorption results, as discussed earlier. Note that some of the intermediate states such as Mn^{5+} and Mn^{2+} are shown to be well within the conduction band (CB) or valence band (VB). In Mn_2O_3, for instance, Mn^{4+} is both a native defect (dopant) formed during synthesis as well as an electrochemical intermediate formed during polarization. The Mn^{5+} charge state, on the other hand, forms only during polarization as $Mn^{5+}{=}O^{2-}$ at a potential of 1.55 V versus RHE. Converting this value to the vacuum energy scale, the electron chemical potential of Mn^{5+} was determined to be −5.28 eV at pH = 12. The changes in the band bending occurring during polarization are not shown in Figure 9A for clarity.

We consider the band lineup of Mn_2O_3 and NiO_x to elucidate the formation of active sites and the subsequent charge transfer processes at the interface. Both are p-type semiconductors because of acceptor-type native defects (Mn^{4+} in Mn_2O_3 and Ni^{3+} in NiO_x) in the lattice formed during synthesis. Before contact with the electrolyte, the VB and Fermi level (E_F) of Mn_2O_3 lies above the electron energy of oxygen reaction, $E^0_{ORR/OER}$. Upon contact, a h^+-accumulation region is formed at equilibrium, as shown schematically in Figure 9B, which is enhanced further during anodic polarization. Localization of holes leads to the formation Mn^{4+} polaron sites that not only increase the p-type electronic conductivity (because of polaron hopping) of the oxide but also serve as active sites for the binding of OH^- intermediates. Therefore, from the perspective of electrostatic interactions, higher-valent Mn cations such as Mn^{4+} and Mn^{5+} provide higher stabilization for negatively charged OER intermediates.[50] Because Mn^{4+} (polaron) states in Mn^{3+} lattice sites are acceptor-type defects, it leads to a high metallic p-type surface conductivity at positive polarization. In line with this explanation, the surface conductivity and charge transfer resistance in the impedance analysis were modeled using a single parameter, R_{CT}. In contrast, cathodic polarization would decrease the h^+ concentration and therefore increase the p-type resistance, which is consistent with the formation of an insulating state. However, given its small band gap (E_g = 1.3 eV), moderate cathodic overpotentials will lead to the negative shift of E_F that would result in the passivation of Mn^{4+} acceptor states and lead to the formation of donor-type Mn^{2+} defects that give rise to an inverted region with e^--accumulation in the CB. This high density of e^- gives rise to n-type behavior seen in the M−S measurements seen after cathodic prepolarization. In addition, the higher e^- density of Mn^{2+} compared to Mn^{3+} cation means that they are better e^- donors to adsorbed molecular oxygen. Therefore, ORR catalysis occurs more efficiently on a low-valent Mn^{2+} active site, and the onset of ORR current is not observed until the favorable potential for Mn^{2+} formation is reached. These arguments are supported by calculated values of the binding energy of oxygen on many 3d transition metal oxides by Klier[78] that gives the standard enthalpy change of the reaction $2Mn^{2+}O + 1/2O_2 \rightarrow Mn_2^{3+}O_3$ to be −45 kcal/g, while that of the reaction $Mn_2^{3+}O_3 + 1/2O_2 \rightarrow 2Mn^{4+}O_2$ to be only −19 kcal/g. These values point to the higher affinity of O_2 for the Mn^{2+} cation over Mn^{3+}, which is in part due to the higher crystal field stabilization of Mn^{3+}. Therefore, bifunctional activity of Mn_2O_3 is a result of its ability to form both high-valent (Mn^{4+}) and low-valent (Mn^{2+}) cations that serve as active sites for OER and ORR, respectively.

On the other hand, nonbifunctional oxides (Co_3O_4, NiO_x) show native p-type conductivity because of higher-valent metal cations (Ni^{3+} in NiO_x). The VB of NiO_x lies below $E^0_{ORR/OER}$. This gives rise to a h^+ depletion region on the surface in the pH = 12 electrolyte at equilibrium. Anodic polarization results in an increase in the concentration of higher-valent metal cations (Ni^{3+} in NiO_x), as seen with both NIR-PL and absorbance results, that increases the p-type conductivity and serve as active sites for OER. Therefore, the material shows good activity for OER. However, NiO_x and Co_3O_4, unlike

https://dx.doi.org/10.1021/acs.jpcc.0c00714
J. Phys. Chem. C 2020, 124, 5286−5299

Mn_2O_3, have large band gaps where the CB energy lies at higher energy than the $E^0_{ORR/OER}$. Consequently, cathodic polarization of the oxide from equilibrium further decreases the h^+ concentration, thus passivating Ni^{3+} native acceptor defect states, but cannot shift the Fermi level closer to the CB (no switch in polarity or formation of Ni^{1+}). This inability to form lower-valent, donor-type Ni^{1+}cation active sites means that they show no switch in the electrical polarity (unipolar conductivity) but rather undergo a metal-to-insulator transition during cathodic polarization. They remain p-type but with an insulating phase. Any small ORR activity likely occurs at the Ni^{2+}, which are likely efficient at O_2 binding. These results suggest that the electrocatalytic activity of an oxide is critically dependent on the potential of defect formation.

Using these concepts, one can now define a descriptor based on the relative potential of formation of relevant metal cation defects to correlate with the activity. For instance, an important criterion for the bifunctionality is that the formation potential of both acceptor and donor defects (U^{def}) must occur close to the thermodynamic potential of the redox reaction ($U^0_{ORR/OER}$). The difference, $U^{def} - U^0_{ORR/OER}$, can therefore be used as a descriptor to determine the electrocatalytic activity of an oxide, that is, the ease of the formation of these defects is related to the catalytic activity.

Finally, we note that pH-dependent changes of Mn_2O_3 (Figure S5) can be understood within this band lineup framework. The increase in p-type character of Mn_2O_3 with increasing pH is due to the increased stabilization of OH^--related adsorbates (such as *OH, *O, *OOH) species at higher pH than at lower pH. Consequently, higher Mn oxidation states, such as Mn^{4+}−OOH^- and Mn^{5+}=O^{2-}, are acceptor-type defect states that are more stable at higher pH, which increase the p-type character. Such a surface is highly active for OER or other oxidizing reactions. On the contrary, the increase in the n-type characteristics of Mn_2O_3 with decreasing pH is a result of formation and stabilization of Mn^{2+} states.[24]

CONCLUSIONS

In conclusion, using the novel electrochemical NIR-PL technique for probing cation valence states along with impedance and gravimetric measurements, we have shown the correlation between electrochemical activity, nature of metal cations acting as active sites, and the measured charge transfer and surface resistance. Our results show that good bifunctional activity for both OER and ORR, as seen in α-Mn_2O_3, is due to the catalyst's ability to shuttle between high valence states ($Mn^{4+}$and Mn^{5+}) and a low valence state (Mn^{2+}) that serve as active sites for OER and ORR, respectively. The resulting transitions lead to potential-dependent surface resistance changes. Consequently, there is a switch in the polarity between an n-type phase with Mn^{2+} states and a p-type conducting phase with defects during reduction (ORR) and oxidation (OER), respectively, that are enabled because of low defect formation potentials. In contrast, nonbifunctional oxides (NiO_x, Co_3O_4) have wider band gaps, which cause donor-type defect states to lie outside the electrolyte potential window. Consequently, they show no switch in the electrical polarity and show poor activity for one of the two oxygen reactions. Therefore, an oxide should have a small band gap (<1 eV) with CB and VB edges close to the oxygen redox potential in order for it to be bifunctional. The defect-property function relationships shown here have important implications for the design of both bifunctional and nonbifunctional electrodes relevant for energy-storage devices.

METHODS

Oxide Synthesis and Electrode Preparation. Ruthenium oxide (RuO_2) used in the present study was prepared by thermal decomposition of $RuCl_3 \cdot 6H_2O$ at 450 °C for 3 h. All other oxide powders of various stoichiometries (MnO, α-Mn_2O_3, and α-MnO_2), nickel oxide (NiO_x with $x > 1$), and cobalt oxide (Co_3O_4) used in the present study were purchased from Sigma-Aldrich. Electrodes were prepared by sequential layer-by-layer deposition of a slurry containing oxide powder in dimethyl formamide (DMF) at 80 °C on a GC RDE electrode for electrocatalytic studies and also on FTO-coated glass slides for optical and some electrochemical studies. This process resulted in a continuous, uniform porous oxide films. No conductive binders or fillers were used for electrode preparation as they are known to participate in faradaic reactions at high overpotentials.

Electrochemical Charging. Electrocatalytic testing was done in a three-electrode RDE setup (Pine instruments) with the oxide-coated GC as the working electrode along with Ag/AgCl/saturated KCl and Pt mesh as the reference and counter electrodes, respectively, in an Ar-purged or O_2-purged aqueous electrolyte whose pH was adjusted using KOH and H_2SO_4. The potential of this reference electrode was converted to the RHE scale using the relation $U^{applied}_{RHE} = U^{applied}_{Ag/AgCl} + (0.059*12) + 0.197$. Electrochemical charging was done by applying a linear potential scan using a CH Instruments 660E electrochemical workstation. The current density was calculated based on the weight of the electrode, and the surface area was estimated from BET isotherms. The resistance of the electrode was measured in situ by electrochemical impedance spectroscopy. The total impedance of the cell was measured in the frequency range of 0.1 Hz to 1 MHz at an ac amplitude of 5 mV by interrupting the potential scan at various potentials. To determine the nature of majority charge carriers at a given dc potential, M−S measurements were performed on the electrode in the same electrolyte. The capacitance of the electrode was determined at a fixed ac frequency of 1000 Hz as a function of the scan voltage after prepolarization at the anode (2.1 V) and cathode (0 V) for 10−30 min until steady-state current was reached. The uncompensated charge carrier concentration, N_D, and the flat band potential were estimated through the M−S analysis using the equation

$$\frac{1}{C^2} = \frac{2\left[\left(V_{FB} - \frac{kT}{q}\right) - V\right]}{q\varepsilon_s N_D}$$

Here, C is the measured capacitance at applied voltage V, ε_s is the permittivity of Mn_2O_3 with a value of 5.1,[42] and q is the elementary charge. For measurements recorded in electrolytes of varying pH, a fresh electrode of nearly similar mass and area was used for each of the runs to avoid interference from electrolyte ions.

EQCM Studies. The change in mass on the Mn_2O_3 electrode was recorded in situ using time-resolved EQCM (CH Instruments 400C) that employed an 8 MHz gold-coated resonating quartz crystal. The working electrode for these studies was prepared by drop-casting a thin layer of Mn_2O_3/DMF slurry directly on the Au electrode. Prior to all experiments, the resonator was locked to the resonant

https://dx.doi.org/10.1021/acs.jpcc.0c00714
J. Phys. Chem. C 2020, 124, 5286−5299

frequency of the crystal and permitted to stabilize for 15 min. The change in resonant frequency (Δf) over time was correlated to a change in mass (Δm) on the electrode using the Sauerbrey equation

$$\Delta f = -2f_0^{\,2}/[A(\mu\rho)^{1/2}]\Delta m$$

where f_0 is the resonant frequency of the crystal, A is the area of the gold disk, ρ is the density of quartz (2.648 g/cm^3), and μ is the shear modulus (2.947×10^{11} g/cm s^2) for the quartz. None of the mass changes observed corresponded to a change of greater than 2% of f_0, which validated the use of the Sauerbrey equation for analysis. Comparison of control experiments performed with only the Au substrate in the same electrolyte confirmed that observed mass change corresponded only to that of the oxide and not of the Au substrate.

Optical Studies. In situ changes in the optical absorbance of the Mn_2O_3 and NiO_x electrodes were recorded in the reflectance mode with an integrating sphere using a UV−vis−NIR spectrophotometer (Shimadzu UV-3600) in the range of 300−2700 nm. The three-electrode setup was the same as that used for electrochemical measurements. Absorbance of the electrode was recorded after 20 min of the application of each potential step.

Ex situ photoluminescence and Raman measurements in the range from 330 to 1700 nm were obtained using a HORIBA Scientific LabRAM HR Evolution spectrometer equipped with Si and InGaAs CCD detectors using an excitation wavelength of 325 nm (He−Cd laser) and 633 nm (He−Ne laser). All PL spectra were obtained at room temperature in a reflective backside configuration. The laser power used for sample excitation in the NIR range using 633 nm laser was ∼1.7 mW, while that used in the UV−visible range using 325 nm laser was 7 mW.

X-ray Studies. XPS measurements were done using a Physical Electronics PHI 5000 VersaProbe system comprising a monochromatic Al (Kα) (1486.7 eV) X-ray source and a 150 mm radius hemispherical electron energy analyzer. All spectra are normalized in energy to the C 1s peak. Survey scans were collected over the range from 1100 to 0 eV with a pass energy of 117.4 eV. Typical surveys were collected for 10 min. Higher-resolution scans were collected over a range of 20 eV around the peak of interest with 23.5 eV pass energy. Typical close-up scans were detected for 10−20 min per peak of interest.

■ ASSOCIATED CONTENT

Supporting Information

The Supporting Information is available free of charge at https://pubs.acs.org/doi/10.1021/acs.jpcc.0c00714.

XRD patterns, XPS analysis, electrochemical impedance analysis, PL, and UV−vis absorption results (PDF)

■ AUTHOR INFORMATION

Corresponding Author

Vidhya Chakrapani − *Howard P. Isermann Department of Chemical and Biological Engineering and Department of Physics, Applied Physics, and Astronomy, Rensselaer Polytechnic Institute, Troy, New York 12180, United States;* orcid.org/0000-0003-2682-3833; Email: chakrv@rpi.edu

Authors

Indroneil Roy − *Howard P. Isermann Department of Chemical and Biological Engineering, Rensselaer Polytechnic Institute, Troy, New York 12180, United States*

Qi Wang − *Howard P. Isermann Department of Chemical and Biological Engineering, Rensselaer Polytechnic Institute, Troy, New York 12180, United States*

Complete contact information is available at: https://pubs.acs.org/10.1021/acs.jpcc.0c00714

Notes

The authors declare no competing financial interest.

■ ACKNOWLEDGMENTS

The authors would like to thank Rensselaer Polytechnic Institute (RPI) and National Science Foundation, DMR award (no. 1709649), for the partial financial support and Nicholas Smieszek for his assistance with the preparation of this manuscript. I.R. and Q.W. also gratefully acknowledge the partial support of Howard P. Isermann fellowship provided by the Department of Chemical and Biological Engineering at RPI.

■ REFERENCES

(1) Yang, Z.; Zhang, J.; Kintner-Meyer, M. C. W.; Lu, X.; Choi, D.; Lemmon, J. P.; Liu, J. Electrochemical Energy Storage for Green Grid. *Chem. Rev.* **2011**, *111*, 3577−3613.

(2) Yoo, H. D.; Markevich, E.; Salitra, G.; Sharon, D.; Aurbach, D. On the Challenge of Developing Advanced Technologies for Electrochemical Energy Storage and Conversion. *Mater. Today* **2014**, *17*, 110−121.

(3) Badwal, S. P.; Giddey, S. S.; Munnings, C.; Bhatt, A. I.; Hollenkamp, A. F. Emerging Electrochemical Energy Conversion and Storage Technologies. *Front. Chem.* **2014**, *2*, 79.

(4) Chen, G.; Bare, S. R.; Mallouk, T. E. Development of Supported Bifunctional Electrocatalysts for Unitized Regenerative Fuel Cells. *J. Electrochem. Soc.* **2002**, *149*, A1092−A1099.

(5) Horkans, J.; Shafer, M. An Investigation of the Electrochemistry of a Series of Metal Dioxides with Rutile-type Structure: MoO_2, WO_2, ReO_2, RuO_2, OsO_2, and IrO_2. *J. Electrochem. Soc.* **1977**, *124*, 1202−1207.

(6) Maiyalagan, T.; Jarvis, K. A.; Therese, S.; Ferreira, P. J.; Manthiram, A. Spinel-type Lithium Cobalt Oxide as a Bifunctional Electrocatalyst for the Oxygen Evolution and Oxygen Reduction Reactions. *Nat. Commun.* **2014**, *5*, 3949.

(7) Hosseini-Benhangi, P.; Garcia-Contreras, M. A.; Alfantazi, A.; Gyenge, E. L. Method for Enhancing the Bifunctional Activity and Durability of Oxygen Electrodes with Mixed Oxide Electrocatalysts: Potential Driven Intercalation of Potassium. *J. Electrochem. Soc.* **2015**, *162*, F1356−F1366.

(8) Lu, Y.-C.; Xu, Z.; Gasteiger, H. A.; Chen, S.; Hamad-Schifferli, K.; Shao-Horn, Y. Platinum−Gold Nanoparticles: A Highly Active Bifunctional Electrocatalyst for Rechargeable Lithium−Air Batteries. *J. Am. Chem. Soc.* **2010**, *132*, 12170−12171.

(9) Chen, G.; Delafuente, D. A.; Sarangapani, S.; Mallouk, T. E. Combinatorial Discovery of Bifunctional Oxygen Reduction — Water Oxidation Electrocatalysts for Regenerative Fuel Cells. *Cat. Today* **2001**, *67*, 341−355.

(10) Yim, S.-D.; Lee, W.-Y.; Yoon, Y.-G.; Sohn, Y.-J.; Park, G.-G.; Yang, T.-H.; Kim, C.-S. Optimization of Bifunctional Electrocatalyst for PEM Unitized Regenerative Fuel Cell. *Electrochim. Acta* **2004**, *50*, 713−718.

(11) Zhang, J.; Zhao, Z.; Xia, Z.; Dai, L. A Metal-free Bifunctional Electrocatalyst for Oxygen Reduction and Oxygen Evolution Reactions. *Nat. Nanotechnol.* **2015**, *10*, 444.

(12) Liang, Y.; Li, Y.; Wang, H.; Zhou, J.; Wang, J.; Regier, T.; Dai, H. Co_3O_4 Nanocrystals on Graphene as a Synergistic Catalyst for Oxygen Reduction Reaction. *Nat. Mater.* **2011**, *10*, 780.
(13) Liu, S.; Li, L.; Ahn, H. S.; Manthiram, A. Delineating the Roles of Co_3O_4 and N-doped Carbon Nanoweb (CNW) in Bifunctional Co_3O_4/CNW Catalysts for Oxygen Reduction and Oxygen Evolution Reactions. *J. Mater. Chem. A* **2015**, *3*, 11615−11623.
(14) Aijaz, A.; Masa, J.; Rösler, C.; Xia, W.; Weide, P.; Botz, A. J. R.; Fischer, R. A.; Schuhmann, W.; Muhler, M. Co@Co_3O_4 Encapsulated in Carbon Nanotube-Grafted Nitrogen-Doped Carbon Polyhedra as an Advanced Bifunctional Oxygen Electrode. *Angew. Chem., Int. Ed.* **2016**, *55*, 4087−4091.
(15) Benbow, E. M.; Kelly, S. P.; Zhao, L.; Reutenauer, J. W.; Suib, S. L. Oxygen Reduction Properties of Bifunctional α-Manganese Oxide Electrocatalysts in Aqueous and Organic Electrolytes. *J. Phys. Chem. C* **2011**, *115*, 22009−22017.
(16) Meng, Y.; Song, W.; Huang, H.; Ren, Z.; Chen, S.-Y.; Suib, S. L. Structure−Property Relationship of Bifunctional MnO_2 Nanostructures: Highly Efficient, Ultra-Stable Electrochemical Water Oxidation and Oxygen Reduction Reaction Catalysts Identified in Alkaline Media. *J. Am. Chem. Soc.* **2014**, *136*, 11452−11464.
(17) Ohsaka, T.; Mao, L.; Arihara, K.; Sotomura, T. Bifunctional Catalytic Activity of Manganese Oxide Toward O_2 Reduction: Novel Insight into the Mechanism of Alkaline Air Electrode. *Electrochem. Commun.* **2004**, *6*, 273−277.
(18) Hardin, W. G.; Slanac, D. A.; Wang, X.; Dai, S.; Johnston, K. P.; Stevenson, K. J. Highly Active, Nonprecious Metal Perovskite Electrocatalysts for Bifunctional Metal−Air Battery Electrodes. *J. Phys. Chem. Lett.* **2013**, *4*, 1254−1259.
(19) Wang, L.; Stoerzinger, K. A.; Chang, L.; Zhao, J.; Li, Y.; Tang, C. S.; Yin, X.; Bowden, M. E.; Yang, Z.; Guo, H.; You, L.; Guo, R.; Wang, J.; Ibrahim, K.; Chen, J.; Rusydi, A.; Wang, J.; Chambers, S. A.; Du, Y. Tuning Bifunctional Oxygen Electrocatalysts by Changing the A-Site Rare-Earth Element in Perovskite Nickelates. *Adv. Funct. Mater.* **2018**, *28*, 1803712.
(20) Müller, S.; Striebel, K.; Haas, O. $La_{0.6}Ca_{0.4}CoO_3$: A Stable and Powerful Catalyst for Bifunctional Air Electrodes. *Electrochim. Acta* **1994**, *39*, 1661−1668.
(21) Nikolova, V.; Iliev, P.; Petrov, K.; Vitanov, T.; Zhecheva, E.; Stoyanova, R.; Valov, I.; Stoychev, D. Electrocatalysts for Bifunctional Oxygen/Air Electrodes. *J. Power Sources* **2008**, *185*, 727−733.
(22) Zhu, Y.; Su, C.; Xu, X.; Zhou, W.; Ran, R.; Shao, Z. A Universal and Facile Way for the Development of Superior Bifunctional Electrocatalysts for Oxygen Reduction and Evolution Reactions Utilizing the Synergistic Effect. *Chem.—Eur. J.* **2014**, *20*, 15533−15542.
(23) Gorlin, Y.; Jaramillo, T. F. A Bifunctional Nonprecious Metal Catalyst for Oxygen Reduction and Water Oxidation. *J. Am. Chem. Soc.* **2010**, *132*, 13612−13614.
(24) Su, H.-Y.; Gorlin, Y.; Man, I. C.; Calle-Vallejo, F.; Nørskov, J. K.; Jaramillo, T. F.; Rossmeisl, J. Identifying Active Surface Phases for Metal Oxide Electrocatalysts: A Study of Manganese Oxide Bifunctional Catalysts for Oxygen Reduction and Water Oxidation Catalysis. *Phys. Chem. Chem. Phys.* **2012**, *14*, 14010−14022.
(25) Ramírez, A.; Hillebrand, P.; Stellmach, D.; May, M. M.; Bogdanoff, P.; Fiechter, S. Evaluation of MnO_x, Mn_2O_3, and Mn_3O_4 Electrodeposited Films for the Oxygen Evolution Reaction of Water. *J. Phys. Chem. C* **2014**, *118*, 14073−14081.
(26) Schöfberger, W.; Faschinger, F.; Chattopadhyay, S.; Bhakta, S.; Mondal, B.; Elemans, J. A. A. W.; Müllegger, S.; Tebi, S.; Koch, R.; Klappenberger, F.; Paszkiewicz, M.; Barth, J. V.; Rauls, E.; Aldahhak, H.; Schmidt, W. G.; Dey, A. A Bifunctional Electrocatalyst for Oxygen Evolution and Oxygen Reduction Reactions in Water. *Angew. Chem., Int. Ed.* **2016**, *55*, 2350−2355.
(27) Smith, P. F.; Deibert, B. J.; Kaushik, S.; Gardner, G.; Hwang, S.; Wang, H.; Al-Sharab, J. F.; Garfunkel, E.; Fabris, L.; Li, J.; Dismukes, G. C. Coordination Geometry and Oxidation State Requirements of Corner-Sharing MnO6 Octahedra for Water Oxidation Catalysis: An Investigation of Manganite (γ-MnOOH). *ACS Catal.* **2016**, *6*, 2089−2099.
(28) Robinson, D. M.; Go, Y. B.; Mui, M.; Gardner, G.; Zhang, Z.; Mastrogiovanni, D.; Garfunkel, E.; Li, J.; Greenblatt, M.; Dismukes, G. C. Photochemical Water Oxidation by Crystalline Polymorphs of Manganese Oxides: Structural Requirements for Catalysis. *J. Am. Chem. Soc.* **2013**, *135*, 3494−3501.
(29) Fernando, A.; Haddock, T.; Aikens, C. M. Theoretical Investigation of Water Oxidation on Fully Saturated Mn_2O_3 and Mn_2O_4 Complexes. *J. Phys. Chem. A* **2016**, *120*, 2480−2492.
(30) Risch, M.; Stoerzinger, K. A.; Han, B.; Regier, T. Z.; Peak, D.; Sayed, S. Y.; Wei, C.; Xu, Z.; Shao-Horn, Y. Redox Processes of Manganese Oxide in Catalyzing Oxygen Evolution and Reduction: An in Situ Soft X-ray Absorption Spectroscopy Study. *J. Phys. Chem. C* **2017**, *121*, 17682−17692.
(31) Gorlin, Y.; Lassalle-Kaiser, B.; Benck, J. D.; Gul, S.; Webb, S. M.; Yachandra, V. K.; Yano, J.; Jaramillo, T. F. In Situ X-ray Absorption Spectroscopy Investigation of a Bifunctional Manganese Oxide Catalyst with High Activity for Electrochemical Water Oxidation and Oxygen Reduction. *J. Am. Chem. Soc.* **2013**, *135*, 8525−8534.
(32) Rashmi-Rekha; Pal, S.; Gupta, R. P. Calculation of the Multiple Structure of Core p-Vacancy Levels in the Crystal Field. *Phys. Rev. B: Solid State* **1982**, *26*, 35.
(33) Manceau, A.; Gorshkov, A. I.; Drits, V. A. Structural Chemistry of Mn, Fe, Co, and Ni in Manganese Hydrous Oxides; Part I, Information from XANES Spectroscopy. *Am. Mineral.* **1992**, *77*, 1133−1143.
(34) Biesinger, M. C.; Payne, B. P.; Grosvenor, A. P.; Lau, L. W. M.; Gerson, A. R.; Smart, R. S. C. Resolving Surface Chemical States in XPS Analysis of First Row Transition Metals, Oxides and Hydroxides: Cr, Mn, Fe, Co and Ni. *Appl. Surf. Sci.* **2011**, *257*, 2717−2730.
(35) Gupta, R. P.; Sen, S. K. Calculation of Multiplet Structure of Core *p*-vacancy Levels. *Phys. Rev. B: Solid State* **1974**, *10*, 71−77.
(36) Gupta, R. P.; Sen, S. K. Calculation of Multiplet Structure of Core *p*-vacancy Levels. II. *Phys. Rev. B: Solid State* **1975**, *12*, 15−19.
(37) Huynh, M.; Shi, C.; Billinge, S. J. L.; Nocera, D. G. Nature of Activated Manganese Oxide for Oxygen Evolution. *J. Am. Chem. Soc.* **2015**, *137*, 14887−14904.
(38) Nesbitt, H. W.; Banerjee, D. Interpretation of XPS Mn (2p) Spectra of Mn Oxyhydroxides and Constraints on the Mechanism of MnO_2 Precipitation. *Am. Mineral.* **1998**, *83*, 305−315.
(39) Grosvenor, A. P.; Biesinger, M. C.; Smart, R. S. C.; McIntyre, N. S. New Interpretations of XPS Spectra of Nickel Metal and Oxides. *Surf. Sci.* **2006**, *600*, 1771−1779.
(40) Grosvenor, A. P.; Kobe, B. A.; Biesinger, M. C.; McIntyre, N. S. Investigation of Multiplet Splitting of Fe 2p XPS Spectra and Bonding in Iron Compounds. *Surf. Interface Anal.* **2004**, *36*, 1564−1574.
(41) Wang, Q.; Puntambekar, A.; Chakrapani, V. Vacancy-induced Semiconductor-Insulator-Metal Transitions in Non-Stoichiometric Nickel and Tungsten Oxides. *Nano Lett.* **2016**, *16*, 7067−7077.
(42) Dakhel, A. A. Correlated Structural and Electrical Properties of Thin Manganese Oxide Films. *Thin Solid Films* **2006**, *496*, 353−359.
(43) Wang, Q.; Puntambekar, A.; Chakrapani, V. Gaseous Reactions in Adsorbed Water Present on Transition Metal Oxides. *J. Phys. Chem. C* **2017**, *121*, 13151−13163.
(44) Kocha, S. S.; Shinozaki, K.; Zack, J. W.; Myers, D. J.; Kariuki, N. N.; Nowicki, T.; Stamenkovic, V.; Kang, Y.; Li, D.; Papageorgopoulos, D. Best Practices and Testing Protocols for Benchmarking ORR Activities of Fuel Cell Electrocatalysts Using Rotating Disk Electrode. *Electrocatalysis* **2017**, *8*, 366−374.
(45) Tammeveski, K.; Arulepp, M.; Tenno, T.; Ferrater, C.; Claret, J. Oxygen Electroreduction on Titanium-supported Thin Pt Films in Alkaline Solution. *Electrochim. Acta* **1997**, *42*, 2961−2967.
(46) Park, S.-M.; Ho, S.; Aruliah, S.; Weber, M. F.; Ward, C. A.; Venter, R. D.; Srinivasan, S. Electrochemical Reduction of Oxygen at Platinum Electrodes in KOH Solutions-Temperature and Concentration Effects. *J. Electrochem. Soc.* **1986**, *133*, 1641−1649.

https://dx.doi.org/10.1021/acs.jpcc.0c00714
J. Phys. Chem. C 2020, 124, 5286−5299

(47) Couturier, G.; Kirk, D. W.; Hyde, P. J.; Srinivasan, S. Electrocatalysis of the Hydrogen Oxidation and of the Oxygen Reduction Reactions of Pt and Some Alloys in Alkaline Medium. *Electrochim. Acta* **1987**, *32*, 995−1005.
(48) Zinola, C. F.; Luna, A. M.; Castro Luna, W. E.; Arvia, A. J. Kinetics and Mechanism of the Electrochemical Reduction of Molecular Oxygen on Platinum in KOH: Influence of Preferred Crystallographic Orientation. *J. Appl. Electrochem.* **1994**, *24*, 531−541.
(49) Stoerzinger, K. A.; Diaz-Morales, O.; Kolb, M.; Rao, R. R.; Frydendal, R.; Qiao, L.; Wang, X. R.; Halck, N. B.; Rossmeisl, J.; Hansen, H. A.; Vegge, T.; Stephens, I. E. L.; Koper, M. T. M.; Shao-Horn, Y. Orientation-Dependent Oxygen Evolution on RuO_2 Without Lattice Exchange. *ACS Energy Lett.* **2017**, *2*, 876−881.
(50) Gottesfeld, S.; Srinivasan, S. Electrochemical and Optical Studies of Thick Oxide Layers on Iridium and Their Electrocatalytic Activities for the Oxygen Evolution Reaction. *J. Electroanal. Chem. Interfacial Electrochem.* **1978**, *86*, 89−104.
(51) Bard, A. J.; Memming, R.; Miller, B. Terminology in Semiconductor Electrochemistry and Photoelectrochemical Energy Conversion. *Pure Appl. Chem.* **1991**, *63*, 569−596.
(52) Bernard, M.-C.; Hugot-Le Goff, A.; Thi, B. V.; de Torresi, S. C. Electrochromic Reactions in Manganese Oxides I. Raman Analysis. *J. Electrochem. Soc.* **1993**, *140*, 3065−3070.
(53) Ginsburg, A.; Keller, D. A.; Barad, H.-N.; Rietwyk, K.; Bouhadana, Y.; Anderson, A.; Zaban, A. One-step Synthesis of Crystalline Mn_2O_3 Thin Film by Ultrasonic Spray Pyrolysis. *Thin Solid Films* **2016**, *615*, 261−264.
(54) Mo, Y.; Stefan, I. C.; Cai, W.-B.; Dong, J.; Carey, P.; Scherson, D. A. In Situ Iridium LIII-Edge X-ray Absorption and Surface Enhanced Raman Spectroscopy of Electrodeposited Iridium Oxide Films in Aqueous Electrolytes. *J. Phys. Chem. B* **2002**, *106*, 3681−3686.
(55) Hardcastle, F. D.; Wachs, I. E. Determination of the Molecular Structures of Tungstates by Raman Spectroscopy. *J. Raman Spectrosc.* **1995**, *26*, 397−405.
(56) Gosztola, D.; Weaver, M. J. Electroinduced Structural Changes in Manganese Dioxide+Manganese Hydroxide Films as Characterized by Real-time Surface-Enhanced Raman Spectroscopy. *J. Electroanal. Chem. Interfacial Electrochem.* **1989**, *271*, 141−154.
(57) Wu, B. L.; Lincot, D.; Vedel, J.; Yu, L. T. Voltammetric and Electrogravimetric Study of Manganese Dioxide Thin Film Electrodes. Part 1. Electrodeposited Films. *J. Electroanal. Chem.* **1997**, *420*, 159−165.
(58) Goodenough, J. B.; Manoharan, R.; Paranthaman, M. Surface Protonation and Electrochemical Activity of Oxides in Aqueous Solution. *J. Am. Chem. Soc.* **1990**, *112*, 2076−2082.
(59) Wang, Q.; Brier, M.; Joshi, S.; Puntambekar, A.; Chakrapani, V. Defect Induced Burstein-Moss Shift in reduced V_2O_5 Nanostructures. *Phys. Rev. B* **2016**, *94*, 245305.
(60) Puntambekar, A.; Wang, Q.; Miller, L.; Smieszek, N.; Chakrapani, V. Electrochemical Charging of CdSe Quantum Dots: Effects of Adsorption versus Intercalation. *ACS Nano* **2016**, *10*, 10988−10999.
(61) Sherman, D. M. The Electronic Structures of Manganese Oxide Minerals. *Am. Mineral.* **1984**, *69*, 788−799.
(62) Mićić, R.; Drašković, B. Some Photoluminescence Properties of Mn^{2+} in Magnesium Bromide. *Phys. Status Solidi B* **1985**, *128*, 489−494.
(63) Sekiguchi, D.; Adachi, S. Synthesis and Photoluminescence Spectroscopy of $BaGeF_6$:Mn^{4+} Red Phosphor. *Opt. Mater.* **2015**, *42*, 417−422.
(64) Silva, A. S.; Lourenço, S. A.; Dantas, N. O. Mn Concentration-Dependent Tuning of Mn^{2+} d Emission of $Zn_{1-x}Mn_xTe$ Nanocrystals Grown in a Glass System. *Phys. Chem. Chem. Phys.* **2016**, *18*, 6069−6076.
(65) Ren, H.; Yang, F. Influence of Mn^{2+} on the Up-Conversion Emission Performance of Mn^{2+}, Yb^{3+}, Er^{3+}: $ZnWO_4$ Green Phosphors. *J. Mater. Sci.* **2018**, *29*, 15396.
(66) Verdun, H. R. In Absorption and Emission Properties of the New Laser-Active Center in Mn^{5+} in Several Crystalline Hosts, *Advanced Solid State Lasers*; Optical Society of America, 1993; p TL7.
(67) Cao, R.; Qiu, J.; Yu, X.; Sun, X. Spectroscopic Investigation on $BaSO_4$:(Mn^{6+}, Mn^{5+}) Crystal. *ECS J. Solid State Sci. Technol.* **2013**, *2*, R237−R240.
(68) Najafpour, M. M.; Renger, G.; Hołyńska, M.; Moghaddam, A. N.; Aro, E.-M.; Carpentier, R.; Nishihara, H.; Eaton-Rye, J. J.; Shen, J.-R.; Allakhverdiev, S. I. Manganese Compounds as Water-Oxidizing Catalysts: From the Natural Water-Oxidizing Complex to Nanosized Manganese Oxide Structures. *Chem. Rev.* **2016**, *116*, 2886−2936.
(69) Dau, H.; Limberg, C.; Reier, T.; Risch, M.; Roggan, S.; Strasser, P. The Mechanism of Water Oxidation: From Electrolysis via Homogeneous to Biological Catalysis. *ChemCatChem* **2010**, *2*, 724−761.
(70) Yeo, B. S.; Bell, A. T. In situ Raman Study of Nickel Oxide and Gold-supported Nickel Oxide Catalysts for the Electrochemical Evolution of Oxygen. *J. Phys. Chem. C* **2012**, *116*, 8394−8400.
(71) Jee, J.-E.; Pestovsky, O.; Bakac, A. Preparation and Characterization of Manganese(iv) in Aqueous Acetic Acid. *Dalton Trans.* **2010**, *39*, 11636−11642.
(72) Takashima, T.; Hashimoto, K.; Nakamura, R. Mechanisms of pH-Dependent Activity for Water Oxidation to Molecular Oxygen by MnO_2 Electrocatalysts. *J. Am. Chem. Soc.* **2012**, *134*, 1519−1527.
(73) Perry, C. C.; Li, X. Structural Studies of Gel Phases. Part 2.-Infrared Spectroscopic Study of Silica Monoliths; The Interaction of Water with Surface Species. *J. Chem. Soc., Faraday Trans.* **1991**, *87*, 3857−3862.
(74) Takeuchi, M.; Martra, G.; Coluccia, S.; Anpo, M. Evaluation of the Adsorption States of H_2O on Oxide Surfaces by Vibrational Absorption: Near- and Mid-Infrared Spectroscopy. *J. Near Infrared Spectrosc.* **2009**, *17*, 373−384.
(75) Anderson, J. H.; Wickersheim, K. A. Near Infrared Characterization of Water and Hydroxyl Groups on Silica Surfaces. *Surf. Sci.* **1964**, *2*, 252−260.
(76) Mao, L.; Zhang, D.; Sotomura, T.; Nakatsu, K.; Koshiba, N.; Ohsaka, T. Mechanistic Study of the Reduction of Oxygen in Air Electrode with Manganese Oxides as Electrocatalysts. *Electrochim. Acta* **2003**, *48*, 1015−1021.
(77) Roche, I.; Chaînet, E.; Chatenet, M.; Vondrák, J. Durability of Carbon-Supported Manganese Oxide Nanoparticles for the Oxygen Reduction Reaction (ORR) in Alkaline Medium. *J. Appl. Electrochem.* **2008**, *38*, 1195−1201.
(78) Klier, K. Oxidation-Reduction Potentials and Their Relation to the Catalytic Activity of Transition Metal Oxides. *J. Catal.* **1967**, *8*, 14−21.

https://dx.doi.org/10.1021/acs.jpcc.0c00714
J. Phys. Chem. C 2020, 124, 5286−5299